Binary Volume Acoustic Holograms

Michael D. Brown,[1,2,*] Ben T. Cox,[1] and Bradley E. Treeby[1]

[1]*Department of Medical Physics and Biomedical Engineering, University College London, Gower Street, London WC1E 6BT, United Kingdom*

[2]*Department of Neuroscience, Erasmus MC, NL-3000 CA Rotterdam, Kingdom of the Netherlands*

In recent years, high-resolution additive manufacturing has enabled a diverse range of low-cost methods for ultrasonic wave-front shaping. Acoustic holograms, in particular, allow for the generation of arbitrary diffraction-limited acoustic fields at megahertz frequencies from single-element transducers. These are phase plates that function as direct acoustic analogs to thin optical holograms. In this work, it is shown that, by using multiple polymer three-dimensional (3D) printing, two-material (binary) acoustic analogs to "thick" or volume optical holograms can also be generated. First, an analytic approach for designing a volume hologram that diffracts a set of input fields onto a desired set of output fields is briefly summarized. Next, a greedy-optimization approach based on random downhill binary search able to account for the constraints imposed by the chosen fabrication method is introduced. Finally, an experimental test case designed to diffract the field generated by a 2.54-cm planar lead zirconate titanate (PZT) transducer onto eight distinct patterns dependent on the direction of the incident field is used to validate the approach and the design method. Field scans of the eight target fields demonstrate that acoustic analogs of optical volume holograms can be generated using multipolymer printing and that these allow the multiplexing of distinct fields onto different incident field directions.

I. INTRODUCTION

The ability to precisely shape and focus acoustic fields is essential to a range of applications in biomedical ultrasound [1–4]. For transcranial ultrasound neuromodulation, for example, such control is required to precisely compensate for the distortions introduced by propagation through the skull [5]. In most existing systems, these corrections are achieved via arrays of independent sources; however, increasingly, there is interest in the potential of passive acoustic metamaterials [6] and lenses [4,7] as a cheaper simpler alternative for transcranial focusing and other biomedical applications. For airborne sound, research has focused on the development of transmission and reflection metasurfaces comprised of subwavelength unit cells with complex internal structures engineered to produce a desired, potentially tunable, phase and/or amplitude modulation [8–10]. For underwater applications, however, due to the differences in impedance contrast and wavelength

compared to airborne sound, research has focused principally on phase-conjugate lenses or acoustic holograms [1,11]. These are phase plates, often three-dimensionally (3D) printed, that can map the continuous-wave output of a single-element transducer onto a precomputed phase pattern via variations in thickness. This phase pattern subsequently diffracts to form a desired field.

Acoustic holograms are cheap to fabricate and offer higher spatial fidelity over the transmitted field than traditional arrays; however, they are static. Each hologram generates a fixed distribution and, as such, their flexibility is limited. To circumvent this, two methods have been introduced. Spatial steering and scaling of a fixed field by modifying the driving frequency or through the use of a coarse array has been reported in several works [12–14]. However, the range available to frequency-based steering is limited by the increasing coupling of energy into different diffraction orders [15], while steering using an array requires more complex driving electronics, is subject to distortions from grating lobes if insufficiently sampled, and is redundant for fully sampled arrays. Alternatively, the frequency dependence of the phase delay introduced by a hologram has been exploited to multiplex distinct patterns onto different driving frequencies [16]. However, this approach is limited by crosstalk between target patterns and the limited transducer bandwidth. Recent works have demonstrated dynamic equivalents to these holographic

_____

*Michael.brown.13@ucl.ac.uk

(a)   **(b)**

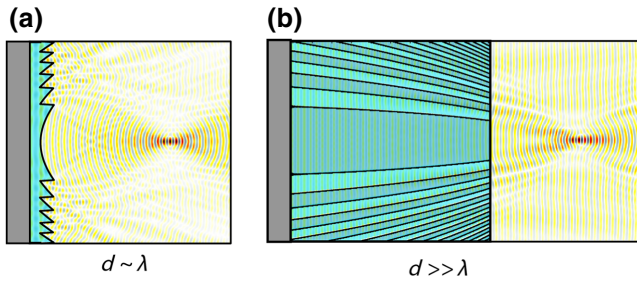$d \sim \lambda$ $d \gg \lambda$

FIG. 1.   (a) The visualization of a thin acoustic hologram that shapes the field by acting as a thin phase screen. (b) The visualization of a thick volume acoustic hologram that shapes the field through scattering from sound-speed variations.

lenses in the form of rewritable bubble masks generated via electrolysis or optically induced electrochemical interactions [17,18]. However, these approaches have higher cost and technical complexity and, at present, have only demonstrated the capacity for binary amplitude modulation of an incident field limiting the efficiency with which energy can be coupled into the desired field to 10% [19].

Each of these prior works has investigated "thin" holographic lenses [Fig. 1(a)], with a thickness d on the order of the acoustic wavelength λ, to modulate the transmitted field. Both the design and acoustical behavior of these lenses is directly analogous to thin optical holograms (e.g., as generated using a spatial light modulator). In this work, it is demonstrated that by exploiting multiple polymer 3D printing, it is also possible to generate binary volume acoustic holograms. These are direct acoustic analogs to volume optical holograms, also known as thick or Bragg holograms [Fig. 1(b)]. Rather than thin phase elements, volume holograms are extended structures ($d \gg \lambda$), in which the refractive index or absorption modulates periodically about some bulk value. This extended thickness results in holograms that are significantly more selective to the frequency or direction of the incident field, as only waves that match the Bragg criteria for the hologram diffract [20]. As a result, the ability to multiplex distinct patterns within a single structure is significantly greater (e.g., for optical information storage [21]). This enhanced ability to multiplex in a single fixed lens could improve the flexibility of acoustic holograms for biomedical applications.

II. VOLUME-HOLOGRAM DESIGN

A. Problem statement

The general challenge in designing a volume acoustic hologram can be framed as finding a 3D sound-speed distribution $c(\mathbf{r})$ that maps a set of n input fields $p_i^n(\mathbf{r})$ that vary spatially or spectrally onto a set of n predefined output fields $p_o^n(\mathbf{r})$, where $\mathbf{r}$ is the spatial coordinate (x, y, z). This could be treated analogously to ultrasound tomography

(UST) [22] by using full-waveform inversion to find a set of acoustic properties that minimize the residual between a desired field and the output of a numerical wave-equation solver. However, the incorporation of design constraints such that the values converge to a stable solution that can be physically realized would pose a significant challenge. As such, for this work, a single-scattering (Born) approximation is employed, thereby constraining the problem to searching for a sound-speed distribution $c(\mathbf{r})$ with an average bulk value c_m and a weak perturbation $c_h(\mathbf{r})$ around this bulk value. That is,

$$c(\mathbf{r}) = c_m + c_h(\mathbf{r}). \tag{1}$$

The goal is then to find this perturbation $c_h(\mathbf{r})$ that maps between our desired input and output fields. This reframing allows for the design problem to be significantly simplified.

B. Lossless volume-hologram design

The behavior of volume-hologram gratings has been widely studied in optics, which can be used to inform the design. The earliest rigorous theoretical treatment is coupled-wave theory, developed by Kogelnik [23], which describes the Bragg diffraction of waves from an infinite slab with a finite thickness containing periodic modulations in the refractive index or absorption.

For the simplest case of a transmission hologram mapping an incident plane wave $p_i(\mathbf{r}) = e^{i\mathbf{k}_i \cdot \mathbf{r}}$ with wave vector $\mathbf{k}_i$ onto an output plane wave $p_o(\mathbf{r}) = e^{i\mathbf{k}_o \cdot \mathbf{r}}$ with wave vector $\mathbf{k}_o$, a medium $c_h(\mathbf{r})$ coupling these two fields can be shown to be

$$c_h(\mathbf{r}) = \Re\{e^{i\mathbf{k}_i \cdot \mathbf{r}} e^{-i\mathbf{k}_o \cdot \mathbf{r}} \Delta c\}. \tag{2}$$

Here, Δc is the scaling of the perturbation and $\Re$ denotes the real component. Equation (2) defines a new grating with a wave vector $\mathbf{k}_g$ given by the difference of the two wave vectors,

$$\mathbf{k}_g = \mathbf{k}_i - \mathbf{k}_o. \tag{3}$$

This case is illustrated by Fig. 2, which shows the real component of an incident field p_i (a), an output field p_o (b), and a hologram medium c_h (c) for a case where $\mathbf{k}_i$ is parallel to x (i.e., $\theta_i = 0°$) and $\mathbf{k}_o$ has an angle $\theta_o = 30°$ relative to x. Here, the domain size is 25×25 mm, the frequency f is 2 MHz, and the bulk sound speed c_m is 1484 m s^{-1}.

Assuming that the grating starts in the plane $x = 0$ and that the incident field is the input wave $p_i(\mathbf{r})$, the fraction of energy η in the output wave $p_o(\mathbf{r})$ as a function of the depth
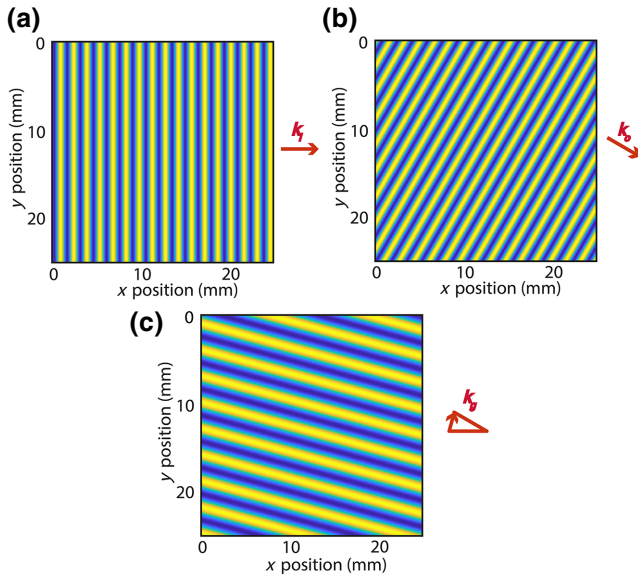
(a)

(b)

(c)

FIG. 2. (a) The real component of the incident plane wave with $\theta_i = 0°$ and frequency 2 MHz. (b) The real component of the output plane wave with $\theta_i = 30°$ and frequency 2 MHz. (c) The sound-speed grating coupling the input (a) and output (b) fields.

x can be calculated, from coupled-wave theory, using [24]

$$\eta(x) = \sin^2\left(\frac{\Delta c}{2c_m}kx(\sec(\theta_i)\sec(\theta_o))^{\frac{1}{2}}\right). \quad (4)$$

Here, $k = |\mathbf{k}_i|$ is the wave number, θ_i is the angle of the incident wave relative to x, θ_o is the angle of the output wave relative to x, and "sec" is the secant function. This assumes that the perturbation $\Delta c < c_m$ (so there is no coupling into higher diffraction orders) and only a single pair of coupled waves. More rigorous models able to exactly account for such effects (e.g., coupling into higher diffraction orders or multiple superimposed gratings) have been reported [20,25]. Equation (4) demonstrates that the fraction of energy coupled into the output field by a volume-hologram grating is determined by the angles of the two plane waves, the magnitude of the sound-speed perturbation, the frequency, and the thickness of the hologram. More generally, with depth, the hologram c_h first couples energy from the incident wave p_i into the output wave p_o and this continues until the incident wave is fully depleted (i.e., all the energy is contained in p_o), after which the grating couples energy back into p_i. This process repeats continually as a function of the depth within the hologram.

This analytic model is compared to a simulation carried out in two dimensions using the k-Wave toolbox, a pseudospectral model for time-domain wave simulations [26]. The contrast magnitude Δc is set to $40\,\text{m s}^{-1}$, the grid spacing is 200 μm, the grid dimensions are 100×100 mm, and the temporal spacing is 27 ns. The fields p_i and p_o and the grating c_h are as shown in Fig. 2. The input field p_i
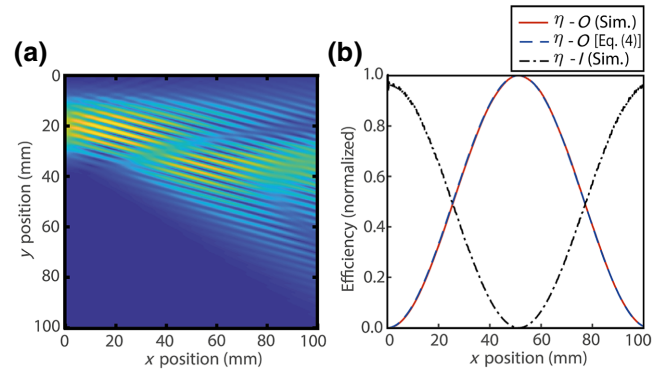
(a)

(b)

FIG. 3. (a) The magnitude of the steady-state field at 2 MHz for the simulated propagation of a normally incident plane wave inside an extension of the grating shown in [Fig. 2(c)]. (b) The energy contained in I and O as a function of the depth within the grating along with the theoretical prediction, demonstrating that, for these example parameters, the assumptions underlying coupled-wave theory are valid.

is inserted as a continuous-wave planar additive source at 2 MHz along $x = 0$, with a width of 40 mm. This is spatially apodized using a Hanning window. The magnitude of the resulting steady-state field at 2 MHz is shown in Fig. 3(a). The coupling between p_i and p_o as a function of the depth x can clearly be seen. The fraction of energy in p_i and p_o is evaluated using a one-dimensional spatial Fourier transform for each depth. The normalized variation of energy p_o compared to the prediction of coupled-wave theory [Eq. (4)] is shown in Fig. 3(b); the two agree almost exactly, showing that the underlying approximations of coupled-wave theory are valid for this Δc.

This approach to designing a volume-hologram grating can be generalized to arbitrary combinations of input and output fields. Assuming that the fields within the volume hologram are represented by their angular spectra $\hat{p}_i(k_x, k_y, k_z)$ and $\hat{p}_o(k_x, k_y, k_z)$, then a hologram coupling the two fields $c_h(x, y, z)$ can be calculated as a weighted sum of gratings [Eq. (2)] using

$$\begin{aligned} c_h(x,y,z) = \Re\Bigg\{\int\cdots\int \\ \hat{p}_i(k_{ix}, k_{iy}, k_{iz})e^{i(k_{ix}x+k_{iy}y+k_{iz}z)} \\ \hat{p}_o(k_{ox}, k_{oy}, k_{oz})e^{-i(k_{ox}x+k_{oy}y+k_{oz}z)} \\ dk_{ix}dk_{iy}dk_{iz}dk_{ox}dk_{oy}dk_{oz}.\Bigg\} \end{aligned} \quad (5)$$

Equation (5) is the Fourier transform of the convolution of the two angular spectra and hence simplifies to a multiplication of the fields in the spatial domain. We can adopt this approach for low-contrast gratings owing to linearity under the Born approximation.
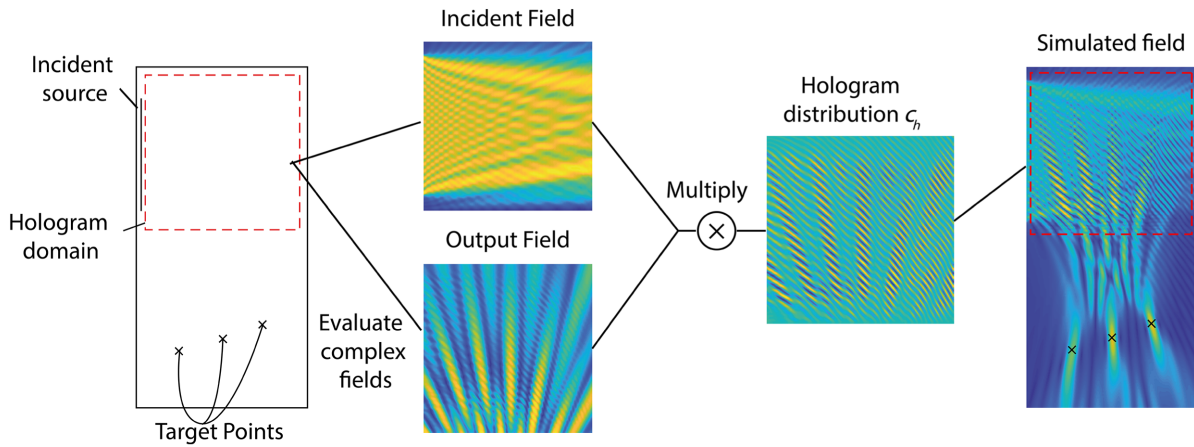
FIG. 4. An illustration of the approach to calculating the volume hologram in a nonabsorbing continuous medium. First, the target field, the input field, and the hologram domain are defined. Next, the incident and target output fields within the hologram domain are calculated; these are then multiplied to calculate c_h. Upon imposing c_h in the simulation domain, the hologram scatters the incident field onto the target field.

The calculation of a hologram with this approach for an arbitrary case is illustrated in Fig. 4. Here, the hologram is two-dimensional (2D), with dimensions of 3×3 cm, the incident field is a planar source with a width of 2.5 cm, and the target field is a set of three focal points, outside the hologram, at differing lateral positions and depths. The design frequency is 2 MHz and c_m is 1484 m s^{-1}. First, the incident and target fields at 2 MHz are calculated within the hologram boundaries. Next, these are spatially multiplied and the real component of the resulting distribution is taken to give the target sound-speed distribution c_h. Finally, upon imposing this sound-speed distribution within the hologram domain, the incident plane wave is mapped onto the desired target distribution.

A key properties of volume holograms is their capacity to multiplex distinct output fields in a single volume. Two types are typically considered; spatial (or angular) multiplexing, where distinct outputs are encoded onto different incident fields (or fields incident from different angles) [27], and frequency multiplexing, where they are encoded onto different driving frequencies [28]. In practice, using a single-scattering assumption, the design of a hologram c_h multiplexing between a distinct set of N input $p_i^n(\mathbf{r})$ and output $p_o^n(\mathbf{r})$ fields can be achieved via a summation of the product of the individual fields. That is,

$$c_h(\mathbf{r}) = \Re\left\{ \sum_{n=1}^{N} p_i^n(\mathbf{r}) p_o^n(\mathbf{r}) \Delta c \right\}. \tag{6}$$

This, however, creates two challenges. First, the diffraction efficiency of each individual field drops by approximately $\sqrt{N}$ [29]. Second, too narrow an angular or wavelength separation results in crosstalk between the different fields. From coupled-wave theory, for the case of coupling two planar waves, the angular and wavelength selectivity are

related to the dimensions of the grating and the angles of the incident and output waves via the following expressions [30]:

$$\Delta\theta_i = \frac{\lambda}{L} \frac{\cos(\theta_o)}{\sin(\theta_i + \theta_o)}, \tag{7}$$

$$\frac{\Delta\lambda}{\lambda} = \frac{\lambda}{L} \frac{\cos(\theta_o)}{1 - \cos(\theta_i + \theta_o)}. \tag{8}$$

Here, $\lambda = 2\pi/k$, and L is the hologram thickness. This, in principle, gives a high degree of selectivity. For example, for $L = 3$ cm, $c_m = 1484$ m s^{-1}, $f = 2$ MHz, $\theta_o = 30°$, and $\theta_i = 0°$. The wavelength selectivity $\Delta\lambda$ is 320 kHz, while the angular selectivity $\Delta\theta_i$ is 2.45°. However, it should be noted that these equations are for a transmission geometry; other geometries (e.g., reflection or 90°) have differing behavior to change in incidence and wavelength [23]. For more complex output fields, the prediction of crosstalk is more involved, requiring analysis of the Ewald spheres of the target fields [31].

III. FABRICATION REQUIREMENTS

The approach outlined in Sec. II B can be used to calculate a volume hologram for diffracting between arbitrary input-output fields in an ideal case where the sound speed can be continuously varied and there is no loss. However, it is not possible to physically realize this at present. The fabrication of an acoustic volume hologram requires the ability to, controllably, spatially vary the mechanical properties of a medium on a length scale on the order of the acoustic wavelength. At 2 MHz, for different plastics, this length scale varies between 0.5 and 1.3 mm, while the mechanical contrast magnitude Δc required varies with the geometry. From Eq. (4), for a 3-cm hologram, with

$\theta_i = 0°, \theta_o = 30°$, and $f = 2$ MHz, with $c_m = 2495$ m s^{-1}, the contrast ratio $\Delta c / c_m$ needs to be approximately 2% or $\Delta c = 50$ m s^{-1} for complete conversion of an incident wave (i.e., 100% diffraction efficiency).

For this work, multipolymer polyjet 3D printing on a Stratasys J835 (Stratasys, Edina, Minnesota, USA) is used for fabrication. This allows for the printing of wide range of materials in a single component with a spatial resolution of < 200 μm. Specifically, the J835 prints "primary" materials Agilus30 (rubberlike) and vero-Clear [poly(methyl methacrylate)-like (i.e., PMMA-like)] and synthesizes a broad range of "derived" materials with mechanical properties varying between these two by depositing predetermined mixtures of the two primary materials [32]. In a recent work [33], the bulk acoustical properties of both of these primary materials as well as several of the derived materials (FLXA9960, FLXA9995, RGDA8625, and RGDA8630) have been characterized, finding the group velocity between 1 and 3.5 MHz to vary between 2019 and 2496 m s^{-1}. However, these values were not distributed continuously over this range, instead being clustered around 2100 m s^{-1} (FLXA9960, FLXA9995, and Agilus30) and 2450 m s^{-1} (RGDA8625, RGDA8630, and VeroClear). In principle, two materials, RGDA8630 (2447 m s^{-1}) and veroClear (2475 m s^{-1}), have sufficient contrast to generate a volume hologram ($\Delta c = 14$ m s^{-1}). In practice, however, such a hologram has been found to be extremely weakly diffracting. As such, to approximate a desired contrast, "mixed" materials have instead been synthesized using random mixtures of Agilus30 ($c = 2035$ m s^{-1}) and veroClear (2475 m s^{-1}) on a 200-μm length scale [34], setting the volume fraction of each material based on the empirically determined desired sound-speed contrast (see Sec. V D).

While multipolymer printing, in principle, offers sufficient fidelity and contrast, its use introduces two additional challenges. First, the losses due to attenuation within the photopolymers at 2 MHz range from 6.3 to 18 dB/cm [33]. Second, the sound-speed distributions that can be fabricated are quantized. For simplicity, in this work, the design of holograms comprised of just two materials—i.e., binary distributions—is considered. These two challenges prohibit the use of a simple lossless model (Sec. III) to design the hologram. Figure 5 shows the effect of both binarization and attenuation on the hologram profile simulated in Fig. 4. The pressure generated over the target points drops and significant variability in the pressure generated over the three focal points is introduced. This variability in the pressure arises principally from attenuation that "apodizes" the grating such that scattering from structures closer to the source is stronger. Simple thresholding of a continuous target distribution also results in overweighting of edges and corners in a target pattern [35]. To account for both attenuation and binarization, a greedy-optimization approach is developed for the design of binary volumetric
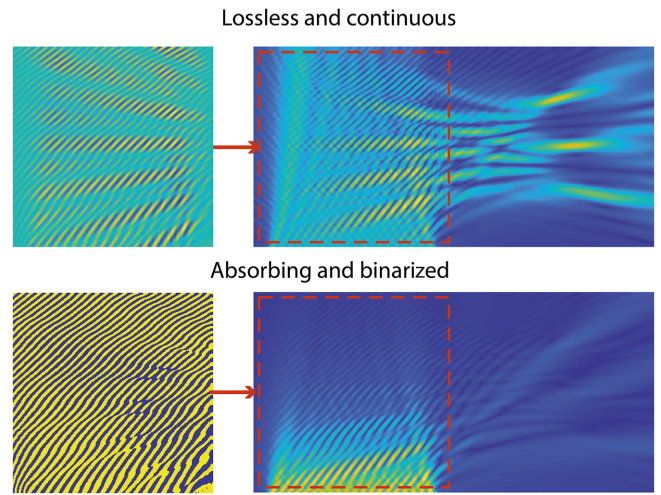

FIG. 5. An illustration of the impact of absorption and binarization on the acoustic field generated by a thick hologram. The attenuation "apodizes" the grating such that scattering from structures close to the source is stronger. Binarization overweights edges and corners.

acoustic holograms in absorbing media. This is an adaptation of an algorithm introduced in several previous works [16,36].

IV. GREEDY DESIGN ALGORITHM

The inverse problem is now to find a binary spatial distribution $h(\mathbf{r})$ that maps a set of continuous-wave input fields described within the hologram as $p_i^n(\mathbf{r})$ onto a set of output target pressure distributions $p_o^n(\mathbf{r})$. These input fields can be defined either for a single frequency f or for a set of distinct frequencies f_n, However, in this work, only a single input frequency is considered.

The hologram is first discretized. For example, a cubic hologram $h(\mathbf{r})$ occupying an $L \times L \times L$ region is represented as a set of evenly spaced points $\mathbf{r}_k = \{(x_k, y_k, z_k), k = 1, \ldots, K\}$, with maximum spacing $\Delta < \lambda/2$ in each dimension to meet the sampling requirements. Here, λ is the wavelength in the hologram medium and the subscript k is the coordinate index. For the definition of arbitrary geometries, the set of points, from a regular grid, are restricted to those that fall within the desired volume. The target distributions p_o^n are also constrained to a single target plane z_d external to the hologram (i.e., $p_o^n = p_o^n(x, y, z_d)$). Additionally, rather than continuous distributions, a set of target points $\mathbf{r}_m^n = \{(x_m, y_m, z_d), m = 1, \ldots, M\}_n$ are instead defined for each output field.

To solve this inverse problem, it is necessary to have a forward model linking each input field $p_i^n(\mathbf{r})$ and hologram state $h(\mathbf{r})$ to the pressure p_m^n generated at each target point

$\mathbf{r}_m^n$. This is modeled as

$$p_m^n = \sum_{k=1}^{K} G_m^n(\mathbf{r}_k) p_i^n(\mathbf{r}_k) h(\mathbf{r}_k). \quad (9)$$

Here, $G_m^n(\mathbf{r}_k)$ is the Green's function between the mth target point of the nth target distribution and the position $\mathbf{r}_k$ inside the hologram, $p_i^n(\mathbf{r}_k)$ is the value of the nth input field at $\mathbf{r}_k$ inside the hologram, and $h(\mathbf{r}_k)$ is the hologram state at the position $\mathbf{r}_k$.

Both $G_m^n(\mathbf{r}_k)$ and $p_i^n(\mathbf{r}_k)$ are precomputed. We consider volume holograms that can have a complex geometry and that are designed to generate target distributions in an external medium (water) that has acoustic properties that differ significantly from the 3D-printed photopolymers. As such, it is necessary to model diffraction, reflection, and attenuation for waves coupling into and out of the hologram when evaluating $G_m^n(\mathbf{r}_k)$ and $p_i^n(\mathbf{r}_k)$. This is accomplished using the k-Wave toolbox, inserting $h(\mathbf{r})$ into the simulation domain as a region with the acoustic properties matching those of the printable photopolymers. However, fully modeling $h(\mathbf{r})$ would require updating $G_m^n(\mathbf{r}_k)$ and $p_i^n(\mathbf{r}_k)$ each time the hologram state is changed. For simplicity, we instead approximate the hologram medium as homogeneous with a bulk sound speed, density, and attenuation (c_m, ρ_m, α_m) defined as the average of the two materials used to fabricate the hologram (i.e., the Green's functions are unaffected by the hologram state $h(\mathbf{r})$). This forward model makes a number of further simplifying assumptions, namely:

(1) The hologram is single scattering.
(2) The incident fields can be neglected at the target points (i.e., $p_i^n(\mathbf{r}_m^n) = 0$).
(3) The hologram is a fluid.
(4) There is no depletion of the incident field by the hologram.
(5) There is no density contrast between the materials.

It is demonstrated experimentally in Sec. V that these assumptions are valid for certain sound-speed contrasts and problem geometries.

The optimization then searches for a binary volume hologram that maximizes the pressure generated over the set of target points for each output field while minimizing the variation in pressure by maximizing the cost function

$$C = E(|p_m^n|) - \beta(std|p_m^n|). \quad (10)$$

Here, p_m^n is the pressure at each target point $\mathbf{r}_m^n$ and α is a weighting parameter. The first term, $E(|p_m^n|)$, is the average pressure over the set of target points for each input field. The second term is the standard deviation of the same parameter. This cost function aims to maximize the energy

over each target distribution while minimizing the variation of pressure. For this work, the value of β is empirically determined and set to 0.7.

The optimization is solved using random downhill binary search. The hologram is initialized in a fully off state $h^0(\mathbf{r})$. From the state $h^l(\mathbf{r})$, the optimization proceeds by selecting a voxel $\mathbf{r}_k$ at random (from those not yet evaluated); this voxel is assigned to the state that maximizes the cost function [Eq. (10)]. This process is then repeated until all voxels have been tested, resulting in an updated hologram $h^{l+1}(\mathbf{r})$. This then repeats until the number of changes in an iteration falls below 0.5% of the number of voxels in the hologram or five iterations are completed.

V. EXPERIMENTAL VALIDATION

A. Introduction

A test case is fabricated to demonstrate that multipolymer printing can be used to realize acoustic analogs of volume holograms and to validate the greedy design algorithm. This is designed to generate the numerals from "1" to "8" for incident fields from eight different directions.
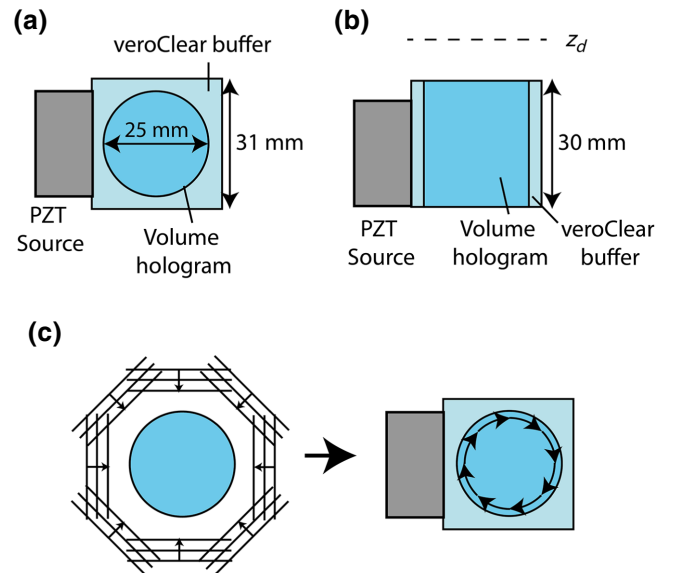

FIG. 6. (a) A top-down view of the geometry of the experimental volume hologram. The test case is a cylindrical hologram of diameter 25 mm, embedded in a $31 \times 31 \times 30$ cm cuboid buffer. (b) A side-on view of the geometry of the experimental volume hologram. (c) An illustration of the approach used to spatially multiplex eight patterns inside the volume-hologram geometry. The cylindrical hologram is able to rotate inside the buffer to change the direction of the incident field from the fixed transducer relative to the hologram. Photographs and renderings of the experimentally fabricated holograms illustrating how this multiplexing works in practice are provided in Fig. 7.
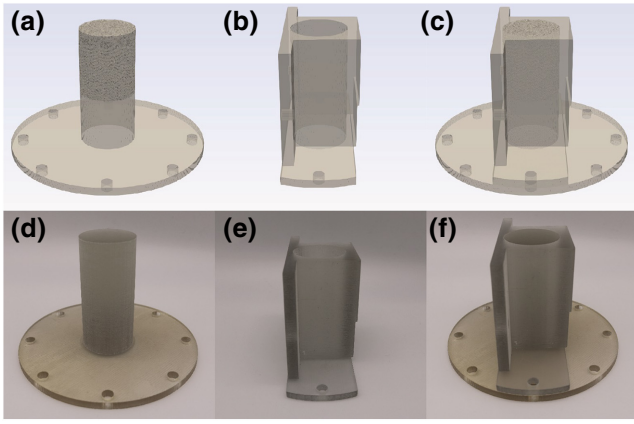
FIG. 7. (a)–(c) Renderings of (a) the multiplexed volume holo-gram, (b) the veroClear holder, and (c) the two models attached to each other. (d)–(f) Photographs of the fabricated models for (d) the volume hologram, (e) the veroClear holder, and (f) the two models attached to each other. In (b) and (e), the PZT trans-ducer is affixed to the (left) side of the veroClear holder, while in (a) and (d), the volume hologram is rotated in 45° increments inside the holder. The target fields are formed over a plane par-allel to the top surface of the volume hologram but spaced away from it by 1 cm.

B. Geometry

The geometry of the test case is illustrated in Fig. 6. Photographs and renderings of the fabricated sample and holder are shown in Fig. 7. The hologram is a cylinder of radius of 2.54 cm and height 3 cm [Figs. 6(a), 6(b), and 7(a)], discretized on a 200-μm grid. This is embedded in a separate $3.14 \times 3.14 \times 3$ cm holder fabricated from veroClear [Figs. 6(a), 6(b), and 7(b)]. The input fields are each generated by a 2.5 cm 2.25 MHz PZT piston trans-ducer (Olympus, Japan). This is attached to one side of the veroClear holder, 5 mm below the top of the cylinder. The target plane is located parallel to the top of the cylinder at a depth of 1 cm [Fig. 6(b)] and the design frequency is 2 MHz. To generate eight distinct input fields from the fixed transducer, the cylindrical hologram is rotated within the buffer in 45° increments, thereby changing the incidence angle of the piston field relative to the hologram [Fig. 6(c)].

C. Hologram calculation

As stated, the target fields consist of the numerals "1" to "8." These are decomposed into a set of 992 target points. Precise calculation of the Green's functions for these tar-get points would require running a large set of full-wave simulations. To avoid this, the hologram-medium–water interface is approximated as an infinite half space, neglect-ing reverberations within the hologram and between the hologram and the veroClear buffer. A single simulation is then used to evaluate the Green's functions for a point

source above this half space. The domain for this simula-tion is a $512 \times 32 \times 240$ grid with a spacing of 200 μm, with a PML size of ten grid points in each dimension. The hologram is inserted as a half space with a height of 3 cm and acoustic properties (c_m, α_m, ρ_m). The rest of the medium is assigned to water. The point source is inserted as a 2-MHz additive source, 1 cm above the interface. The steady-state field $G(d, l)$ as a function of the depth d below the interface and the radial distance l from the source is extracted from this simulation. The values for $G_n^m(\mathbf{r}_k)$ are then calculated from $G(d, l)$ via interpolation.

To calculate the input fields $p_i^n(\mathbf{r}_k)$, the PZT trans-ducer is modeled as a piston with a diameter of 2.54 cm and a uniform apodization and phase. The angular spec-trum method (based on the implementation by Zeng and McGough [37]) is used to propagate this field from 0 to 3 cm on planes spaced by 200 μm. The medium properties are assigned to the bulk properties (c_m, α_m, ρ_m) of the holo-gram. From this 3D volume, the position of each hologram coordinate, $\mathbf{r}_k$, for each input field, is evaluated from the known transducer position and $p_i^n(\mathbf{r}_k)$ is then calculated via interpolation. After evaluation of the input fields and Green's functions, the optimization is run to convergence as outlined in Sec. IV.

D. Hologram contrast

As stated in Sec. III, the materials available by default on the Stratasys J835 have insufficient contrast to realize a volume hologram with high diffraction efficiency. There-fore, "mixed" materials are synthesized using mixtures of Agilus30 ($c = 2035$ m s^{-1}) and veroClear (2475 m s^{-1}) on a 200-μm length scale. The hologram is then fabri-cated from this "mixed" material and veroClear. The target sound-speed contrast, Δc, is 75 m s^{-1}. This is empirically determined by calculating several holograms for the cho-sen geometry and then numerically evaluating their output fields using k-Wave. For contrasts higher than 75 m s^{-1}, it is found that multiple scattering causes the forward model to increasingly break down. This gives a target sound speed for the mixed material of 2325 m s^{-1}, resulting in a mixing ratio of 34% Agilus30 and 66% veroClear. The bulk acous-tic properties (c_m, α_m, ρ_m) used for the hologram design are calculated by averaging the overall volume fraction of Agilus30 and veroClear, assuming a 50:50 mix of the "mixed" material and veroClear. The optimization is then run to convergence for these finalized parameters.

E. Fabrication and measurement

The hologram is next converted into Standard Tessella-tion Language (STL) for printing, along with a model of the veroClear buffer [Figs. 7(a)–7(c)]. Prior to this, a cir-cular ring with radius 45 mm and eight clearance holes spaced by 45° is added to the hologram and two clear-ance holes are added to the buffer to allow them to be
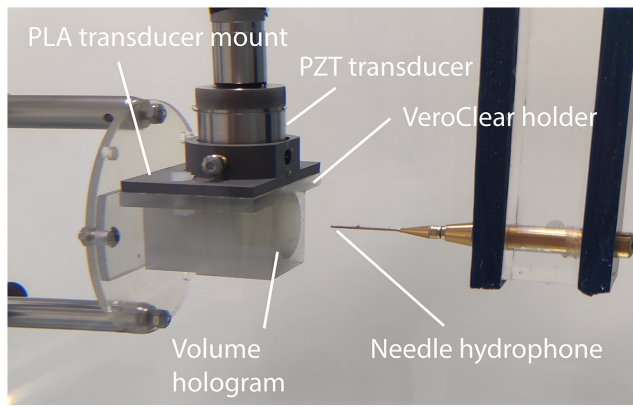
FIG. 8. The experimental setup. The volume hologram [Fig. 7(a)] is inserted into the veroClear holder [Fig. 7(b)] in one of eight predefined positions. The PZT transducer is secured, in the designed position, to one side of the veroClear holder using a PLA mount. A needle hydrophone is then used to record the transmitted field over a plane parallel to the output surface of the volume hologram.

attached with the appropriate set of orientations. Both parts are then fabricated on a Stratasys J835. An additional part, designed to hold the transducer, is printed on an Ultimaker 3 (Ultimaker, Ultrecht, Netherlands) from polylactic acid (PLA).

The output field is measured for each hologram position in a test tank with a three-axis computer-controlled positioning system, using a 0.5-mm needle hydrophone (Precision Acoustics, Dorchester, United Kingdom). The cylindrical hologram is inserted in each of the eight preset positions and the transducer is attached to the veroClear buffer. A photograph of this setup can be seen in Fig. 8. The transducer is driven with a 10 V_{pp} 15-cycle 2 MHz tone burst generated from a signal generator (33522A, Agilent Technologies, Santa Clara, California, USA). The field is recorded over a 30×30 mm area, centered on the middle

of the cylinder, at a depth of approximately 1 cm from the output surface, with a step size of 0.25 mm. Signals are recorded using a M4i.4450-x8 digitizer (Spectrum, Germany), using 64 averages. The acoustic field at 2 MHz is extracted at each measurement position.

Each field scan is compared against a full-wave simulation carried out using the k-Wave toolbox, avoiding the simplifying assumption used to design the volume hologram. These simulations use a $256 \times 256 \times 240$ grid and a step size of 200 μm. The time step is 10 ns and the simulation length is 100 μs. Both the hologram and the veroClear buffer are exactly inserted into the domain (i.e., each voxel is assigned Agilus30 or veroClear rather than approximating the medium with average bulk properties) and the rest of the medium is set to water. The PZT transducer is modeled, in each case, as a 2.54-cm additive piston source with uniform phase and apodization driven at 2 MHz. The time-varying field is recorded over the target plane and the steady-state field at 2 MHz is extracted from each simulation.

F. Measurement results

The experimental (top row) and simulation (bottom row) results for each of the eight target output fields can be seen in Fig. 9. The desired numeral is clearly generated in each experimental data set, confirming both that multipolymer 3D printing can be used to realize acoustic analogs of volume holograms and that the assumptions of the design method are valid. The experimental measurements show good agreement with full-wave simulation, demonstrating that k-Wave can be used to accurately predict the behavior of these volume holograms. There are slightly greater distortions in some of the experimental measurements (e.g., the "1") compared to the simulated results. This could be due to several factors, e.g., inaccuracies in the 3D-printing process, inaccurate modeling of the transducer boundary conditions, or errors in material properties.
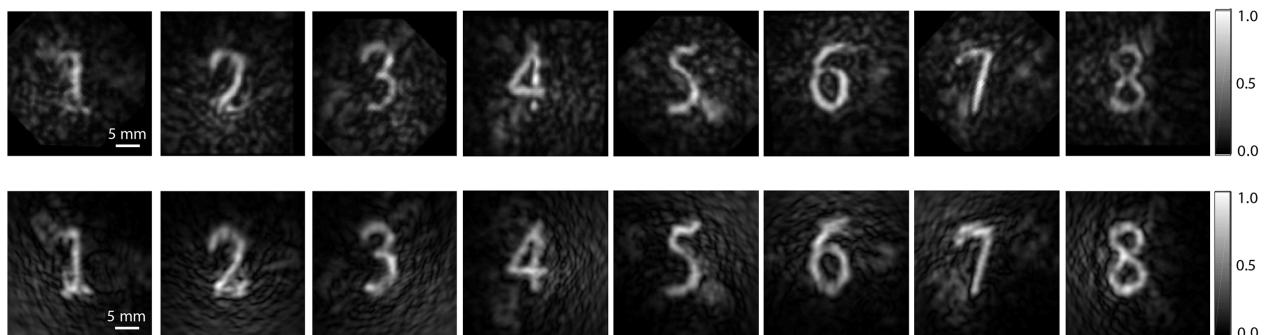

FIG. 9. The normalized experimental and simulated pressure for acoustic fields generated by the binary volume acoustic hologram. Top row: experimental measurements for each of the eight fields at depth of 1 cm from output surface of hologram. Bottom row: simulated results for each of the eight fields at depth of 1 cm from output surface of hologram. Each set of data is normalized to the maximum pressure over the eight fields. Both the simulated and the experimental results generate the desired fields, validating the generation of acoustic analogs of volumetric holograms.

VI. SUMMARY, DISCUSSION AND CONCLUSIONS

This work demonstrates that multiple-polymer 3D printing can be used to realize acoustic analogs to volume holograms and that these enable multiplexing of distinct output fields onto different incident field directions. A one-step algorithm for calculating these volume holograms in continuous media is introduced, along with a greedy-optimization approach capable of designing binary acoustic holograms in absorbing media. Both algorithms rely on a single scattering approximation; however, it is shown experimentally that this holds for low contrast.

The encoding of eight distinct patterns in a single lens is an improvement compared to previous demonstrations using single thin holographic lenses [16]. As such, this could prove useful for applications that already utilize acoustic holograms, such as ultrasound neuromodulation [38] or blood-brain barrier opening [39]. The principal limitation of the approach in this work is the set of approximations employed in the forward model. Future work utilizing approaches analogous to full-wave inversion could bypass this limitation, allowing for higher-fidelity patterns, phase and amplitude control, and a greater ability to multiplex distinct distributions into a fixed lens. The high attenuation of 3D-printable photopolymers also limits the efficiency with which energy can be coupled into the desired fields. In the future, alternative fabrication methods employing materials with lower attenuation could bypass this drawback.

[1] K. Melde, E. Choi, Z. Wu, S. Palagi, T. Qiu, and P. Fischer, Acoustic fabrication via the assembly and fusion of particles, Adv. Mater. **30**, 1704507 (2018).

[2] M. Baudoin, J.-L. Thomas, R. A. Sahely, J.-C. Gerbedoen, Z. Gong, A. Sivery, O. B. Matar, N. Smagin, P. Favreau, and A. Vlandas, Spatially selective manipulation of cells with single-beam acoustical tweezers, Nat. Commun. **11**, 4244 (2020).

[3] P. Kruizinga, P. van der Meulen, A. Fedjajevs, F. Mastik, G. Springeling, N. de Jong, J. G. Bosch, and G. Leus, Compressive 3D ultrasound imaging using a single sensor, Sci. Adv. **3**, e1701423 (2017).

[4] G. Maimbourg, A. Houdouin, T. Deffieux, M. Tanter, and J.-F. Aubry, 3D-printed adaptive acoustic lens as a disruptive technology for transcranial ultrasound therapy using single-element transducers, Phys. Med. Biol. **63**, 025026 (2018).

[5] A. Kyriakou, E. Neufeld, B. Werner, M. M. Paulides, G. Szekely, and N. Kuster, A review of numerical and experimental compensation techniques for skull-induced phase aberrations in transcranial focused ultrasound, Int. J. Hyperthermia **30**, 36 (2014).

[6] G. Memoli, M. Caleap, M. Asakawa, D. R. Sahoo, B. W. Drinkwater, and S. Subramanian, Metamaterial bricks and quantization of meta-surfaces, Nat. Commun. **8**, 14608 (2017).

[7] S. Jiménez-Gambín, N. Jiménez, J. M. Benlloch, and F. Camarena, Holograms to Focus Arbitrary Ultrasonic Fields through the Skull, Phys. Rev. Appl. **12**, 014016 (2019).

[8] S.-W. Fan, Y. Zhu, L. Cao, Y.-F. Wang, A.-L. Chen, A. Merkel, Y.-S. Wang, and B. Assouar, Broadband tunable lossy metasurface with independent amplitude and phase modulations for acoustic holography, Smart Mater. Struct. **29**, 105038 (2020).

[9] Y. Zhu, N. J. Gerard, X. Xia, G. C. Stevenson, L. Cao, S. Fan, C. M. Spadaccini, Y. Jing, and B. Assouar, Systematic design and experimental demonstration of transmission-type multiplexed acoustic metaholograms, Adv. Funct. Mater. **31**, 2101947 (2021).

[10] J. Zhang, Y. Tian, Y. Cheng, and X. Liu, Acoustic holography using composite metasurfaces, Appl. Phys. Lett. **116**, 030501 (2020).

[11] R. J. Lalonde, A. Worthington, and J. W. Hunt, Field conjugate acoustic lenses for ultrasound hyperthermia, IEEE Trans. Ultrason. Ferroelectr. Freq. Control **40**, 592 (1993).

[12] G. Memoli, L. Chisari, J. P. Eccles, M. Caleap, B. W. Drinkwater, and S. Subramanian, in *Proceedings of the 2019 CHI Conference on Human Factors in Computing Systems* (2019), p. 1.

[13] L. Cox, K. Melde, A. Croxford, P. Fischer, and B. W. Drinkwater, Acoustic Hologram Enhanced Phased Arrays for Ultrasonic Particle Manipulation, Phys. Rev. Appl. **12**, 064055 (2019).

[14] R. Lalonde and J. W. Hunt, Variable frequency field conjugate lenses for ultrasound hyperthermia, IEEE Trans. Ultrason. Ferroelectr. Freq. Control **42**, 825 (1995).

[15] M. D. Brown, B. T. Cox, and B. E. Treeby, Stackable acoustic holograms, Appl. Phys. Lett. **116**, 261901 (2020).

[16] M. D. Brown, B. T. Cox, and B. E. Treeby, Design of multi-frequency acoustic kinoforms, Appl. Phys. Lett. **111**, 244101 (2017).

[17] Z. Ma, K. Melde, A. G. Athanassiadis, M. Schau, H. Richter, T. Qiu, and P. Fischer, Spatial ultrasound modulation by digitally controlling microbubble arrays, Nat. Commun. **11**, 4537 (2020).

[18] Z. Ma, H. Joh, D. E. Fan, and P. Fischer, Dynamic ultrasound projector controlled by light, Adv. Sci. **9**, 2104401 (2022).

[19] V. Moreno, J. F. Román, and J. R. Salgueiro, High efficiency diffractive lenses: Deduction of kinoform profile, Am. J. Phys. **65**, 556 (1997).

[20] P. S. J. Russell, Optical volume holography, Phys. Rep. **71**, 209 (1981).

[21] P. J. van Heerden, Theory of optical information storage in solids, Appl. Opt. **2**, 393 (1963).

[22] M. Pérez-Liva, J. Herraiz, J. Udías, E. Miller, B. Cox, and B. Treeby, Time domain reconstruction of sound speed and attenuation in ultrasound computed tomography using full wave inversion, J. Acoust. Soc. Am. **141**, 1595 (2017).

[23] H. Kogelnik, Coupled wave theory for thick hologram gratings, Bell Syst. Tech. J. **48**, 2909 (1969).

[24] B.-R. David, *Understanding Diffraction in Volume Gratings and Holograms* (InTech, Rijeka, 2013).

[25] M. Moharam and T. Gaylord, Rigorous coupled-wave analysis of planar-grating diffraction, JOSA **71**, 811 (1981).

[26] B. E. Treeby and B. T. Cox, k-Wave: MATLAB toolbox for the simulation and reconstruction of photoacoustic wave fields, J. Biomed. Opt. **15**, 021314 (2010).

[27] J. F. Heanue, M. C. Bashaw, and L. Hesselink, Volume holographic storage and retrieval of digital data, Science **265**, 749 (1994).

[28] J. Rosen, M. Segev, and A. Yariv, Wavelength-multiplexed computer-generated volume holography, Opt. Lett. **18**, 744 (1993).

[29] M. Shishova, A. Zherdev, D. Lushnikov, and S. Odinokov, Recording of the multiplexed Bragg diffraction gratings for waveguides using phase mask, Photonics **7**, 97 (2020).

[30] G. W. Burr, Ph.D. thesis, Department of Electrical Engineering, California Institute of Technology, Pasadena (Caltech), 1996, https://thesis.library.caltech.edu/789/.

[31] T. D. Gerke and R. Piestun, Aperiodic volume optics, Nat. Photon. **4**, 188 (2010).

[32] M. Vaezi, S. Chianrabutra, B. Mellor, and S. Yang, Multiple material additive manufacturing—part 1: A review, Virtual Phys. Prototyp. **8**, 19 (2013).

[33] M. Bakaric, P. Miloro, A. Javaherian, B. T. Cox, B. E. Treeby, and M. D. Brown, Measurement of the ultrasound attenuation and dispersion in 3D-printed photopolymer materials from 1 to 3.5 MHz, J. Acoust. Soc. Am. **150**, 2798 (2021).

[34] A. Aghaei, N. Bochud, G. Rosi, Q. Grossman, D. Ruffoni, and S. Naili, Ultrasound characterization of bioinspired functionally graded soft-to-hard composites: Experiment and modeling, J. Acoust. Soc. Am. **151**, 1490 (2022).

[35] P. Tsang, T. Poon, W. Cheung, and J. Liu, Computer generation of binary Fresnel holography, Appl. Opt. **50**, B88 (2011).

[36] M. D. Brown, J. Jaros, B. T. Cox, and B. E. Treeby, Control of broadband optically generated ultrasound pulses using binary amplitude holograms, J. Acoust. Soc. Am. **139**, 1637 (2016).

[37] X. Zeng and R. J. McGough, Evaluation of the angular spectrum approach for simulations of near-field pressures, J. Acoust. Soc. Am. **123**, 68 (2008).

[38] G. Maimbourg, A. Houdouin, T. Deffieux, M. Tanter, and J.-F. Aubry, Steering capabilities of an acoustic lens for transcranial therapy: Numerical and experimental studies, IEEE Trans. Biomed. Eng. **67**, 27 (2019).

[39] S. Jiménez-Gambín, N. Jiménez, A. N. Pouliopoulos, J. M. Benlloch, E. E. Konofagou, and F. Camarena, Acoustic holograms for bilateral blood-brain barrier opening in a mouse model, IEEE Trans. Biomed. Eng. **69**, 1359 (2021).